Applied Surface Science 624 (2023) 157133

Contents lists available at ScienceDirect

Applied Surface Science

journal homepage: www.elsevier.com/locate/apsusc

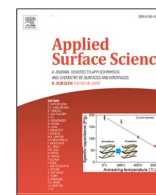

Full Length Article

Suppression of grain boundary contributions on carrier mobility in thin Al-doped ZnO epitaxial films

Riccardo Magrin Maffei [a,b], Alessandro di Bona [a], Maria Sygletou [c], Francesco Bisio [c,d], Sergio D'Addato [a,b], Stefania Benedetti [a,*]

[a] CNR-Istituto Nanoscienze, Via G. Campi 213/a, 41125 Modena, Italy
[b] Dipartimento di Scienze Fisiche, Informatiche e Matematiche, Università di Modena e Reggio Emilia, Via G. Campi 213/a, 41125 Modena, Italy
[c] OptMatLab, Dipartimento di Fisica, Università di Genova, Via Dodecaneso 33, 16146 Genova, Italy
[d] CNR-SPIN, C.so Perrone 24, 16152 Genova, Italy

ARTICLE INFO

Keywords:
Transparent conductive oxides
Thin films
Al-doped ZnO
Epitaxy
Crystalline structure
Electrical properties

ABSTRACT

Realizing very thin transparent conductive (TCO) films is a key aspect of many applications, but often the film quality tends to worsen at very small thicknesses. In this work we demonstrate that Al-doped ZnO (AZO) thin films grown epitaxially on $SrTiO_3$ retain their optimal properties even at thicknesses as low as 30 nm. We deposit by radio frequency magnetron sputtering and investigate the film morphology, structure, crystallinity, electrical and optical properties. We prove that the Hall mobility of epitaxial films is limited mostly by ionized impurity scattering, with a negligible contribution of grain boundary scattering, leading to comparably high mobility in thin epitaxial films. On the contrary, in polycrystalline films the properties of AZO films strongly deteriorate at reduced film thickness, due to grain boundary contributions. The optical carrier density and mobility do not change significantly between epitaxial and polycrystalline films, suggesting that the different electrical properties are indeed mainly due to grain boundary scattering and not to a reduction of carriers and intrinsic mobility. In this way we obtain an epitaxial thin TCO film with the optimal properties of a bulk by a scalable technique, paving the way to applications in plasmonic devices and in thin films solar cells.

1. Introduction

Recently, a great challenge among researchers has been to find a class of materials that combines high optical transparency, typical of insulators, with good electrical conductivity, typical of metals. Materials displaying these properties offer a plethora of applications in fields like photovoltaics, infrared plasmonics and catalysis, optoelectronics, and photonics. One possible answer to this issue is represented by the family of Transparent Conductive Oxides (TCOs), which are highly-doped wide-bandgap semiconductors with electrical and optical properties that can be extensively tuned through doping [1–4].

ZnO is a wide-bandgap semiconductor and when it is doped with Al, it shows a marked *n*-type conductivity, retaining high transparency in the visible range [5,6]. For these reasons and its earth abundance with respect to other TCOs like indium tin oxide (ITO), Al-doped ZnO (AZO) is one of the most interesting and promising materials among TCOs.

For most applications, TCO films are grown as polycrystalline films. It is well known that polycrystalline thin films display lower performances with respect to single crystal materials because they are characterized by far higher concentrations of defects. From an electrical point of view, for instance, a high density of grain boundaries and deep-level defects can trap charge carriers, with a significant detrimental effect on conductivity. In contrast, the control of the interfacial quality between film and support improves the properties of thin films, as in the case of epitaxy or buffer layers [7–9]. In order to fabricate robust and performing optoelectronic devices such as photovoltaic cells [10] or plasmonic devices [11] and in architectures for the modulation of the optical properties of AZO films by external bias [11,12], the epitaxial growth of each layer can be a route to improve efficiency. In these cases the use of a suitable perovskite supporting layer with small lattice mismatch and high dielectric constant is particularly envisaged and could foster epitaxy in AZO, increasing the carrier mobility in the electrode. The effect is particularly important in thin films, where the typical granular composition is constituted by very little grains and the presence of interfaces and grain boundaries dramatically reduces the electrical quality [13,14]. This happens mostly at very low thicknesses,

* Corresponding author.
E-mail address: stefania.benedetti@nano.cnr.it (S. Benedetti).

https://doi.org/10.1016/j.apsusc.2023.157133
Received 31 December 2022; Received in revised form 8 March 2023; Accepted 23 March 2023
Available online 27 March 2023
0169-4332/© 2023 Elsevier B.V. All rights reserved.

where the electrical quality of TCO films, and AZO in particular, degrades [15–18]. For instance, the fabrication of high-quality ultra-thin TCO films would be very important to improve the efficiency of plasmonic-enhanced thin film solar cells, to minimize the parasitic ohmic losses [15,19].

Epitaxial ZnO and AZO films have been grown via various techniques, among which Pulsed Laser Deposition (PLD) [9,20,21] and Laser Molecular Beam Epitaxy (LMBE) [22,23], but very few works about AZO epitaxial growth employing Radio Frequency (RF) magnetron sputtering have been published [8,24,25]. These studies are devoted to the investigation of structural properties of ZnO or AZO on different substrates with a suitable lattice mismatch for epitaxy, like perovskites [20,22,23], sapphire [24,26] and GaN [25], or through a buffer layer [8,9], while in the case of pure ZnO the relation between epitaxy and mobility has been investigated on thick films [27–29].

While thin films grown by RF magnetron sputtering often display a lower quality with respect to films grown by PLD or LMBE, the latter suffer of very low deposition rates and higher costs compared to RF magnetron sputtering, whose scalability is appealing also for industrial applications.

In this work, we present a comprehensive study of the morphological, structural and electrical properties of epitaxial AZO thin films on $SrTiO_3(1\,1\,0)$ grown by RF magnetron sputtering. We show that the improved structural order leads to electrical properties independent on film thickness, being limited only by ionized impurity scattering in very thin epitaxial films. On the contrary, in polycrystalline AZO films grown in the same conditions the electrical properties deteriorate with decreasing thickness.

2. Experimental

AZO films have been deposited by RF magnetron sputtering from an undoped ZnO 3″ target (ZnO purity 99.99 %) about 15 cm far from the substrate in 3×10^{-6} mbar base pressure. 60 W RF power has been applied to the oxide target, corresponding to a final rate of around 0.45 Å/s in an Argon pressure of 5 mTorr. At the same time Al doping was provided by DC magnetron co-sputtering from an Al target, to obtain the optimal doping concentration of 4 at. % [30]. The Al concentration was checked by Energy Dispersive X-ray Spectroscopy (EDX), performed at film surface with a FEI Quanta-200 ESEM. Film thickness is varied between 30 and 300 nm and it has been controlled during deposition by a calibrated quartz microbalance and subsequently by means of a stylus profilometer. The deposition temperature was set to 400 °C by resistive heating and measured with a calibrated thermocouple on the sample stage.

The AZO films have been deposited on $SrTiO_3(1\,1\,0)$ substrates (STO) annealed in vacuum for 3 h at the deposition temperature for degassing before growth. The deposition of AZO on this crystalline plane should be driven by the good matching of the $[\bar{1}10]$ direction of STO ($\sqrt{2}a_{STO}$ = 5.5225 Å) with the $[1\bar{1}00]$ direction of ZnO ($\sqrt{2}a_{ZnO}$ = 5.6288 Å), resulting in a lattice mismatch of 1.9 % [31,32], as shown in Fig. 1. As a reference, we grew polycrystalline AZO films with the same deposition conditions on thermal SiO_2 on Si(0 0 1) substrates.

We investigated the surface morphology of the films with Atomic Force Microscopy (AFM), utilizing an ambient pressure NT-MDT NTEGRA Aura AFM in tapping mode with Si cantilevers. The AFM images have been analyzed with the software *Gwyiddion*.

High-Resolution X-ray Diffraction (HRXRD) measurements have been performed with a PanAnalytical X'Pert Pro four-circle diffractometer (Cu-Kα_1, wavelength 1.5406 Å), equipped with a Göbel mirror in the incidence optics in order to obtain a parallel X-ray beam. The detection optics was comprised of a 0.27° parallel plates collimator, a flat graphite monochromator and a single point gas proportional detector. The goniometer can perform both 2θ-ω scans, where the ω axis follows 2θ at half speed and θ-ω (offset angle) remains constant during the scan, and ω scans, also known as rocking curves, where ω is scanned with 2θ kept constant. The sample was mounted on an Euler cradle that allows independent tilt (ψ) and azimuthal (ϕ) rotations of the sample with respect to the goniometer plane, as shown in Fig. 2. This configuration allows the acquisition of pole figures of selected crystal planes, i.e. the intensity of a given Bragg reflection (constant 2θ) recorded as a function of sample tilt and rotation angles (ψ, ϕ) varied in a large number of orientations.

The electrical properties of the films have been investigated by Van der Pauw and Hall measurements, exploiting aluminum contacts produced via Electron Beam Lithography. The optical response of AZO films was measured by means of variable-angle Spectroscopic Ellipsometry (SE), performed through a J.A. Woollam V-VASE ellipsometer (190–2500 nm spectral range) and a J.A. Woollam M−2000 ellipsometer (245–1700 nm). SE measures the variation of the state of polarization of light reflected off the samples, quantified by the so-called ellipsometric angles Ψ and Δ, defined according to Eq. (1)

$$\frac{r_p}{r_s} = tan(\psi)e^{i\Delta} \tag{1}$$

where r_p and r_s are the complex Fresnel reflection coefficients of the system for p(s)-polarized radiation. The spectra were measured at 60°

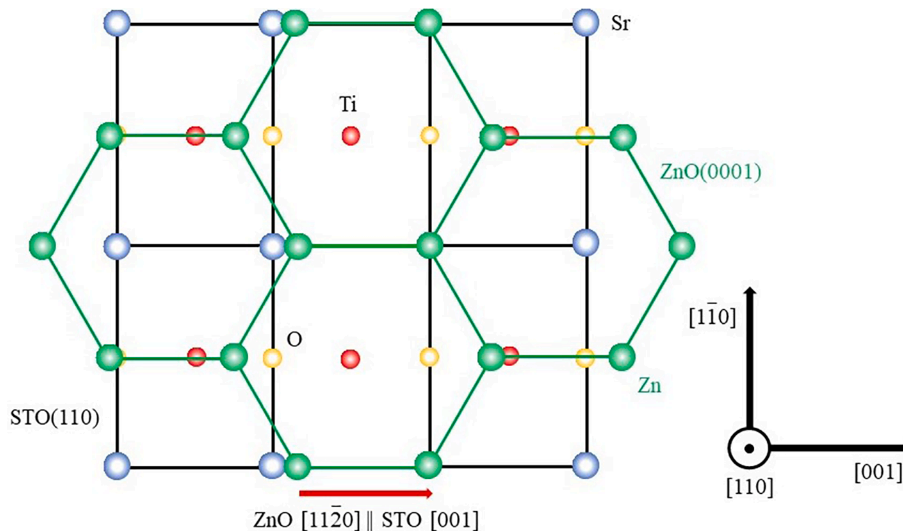

Fig. 1. Expected epitaxial relationship of AZO growth on STO(1 1 0).

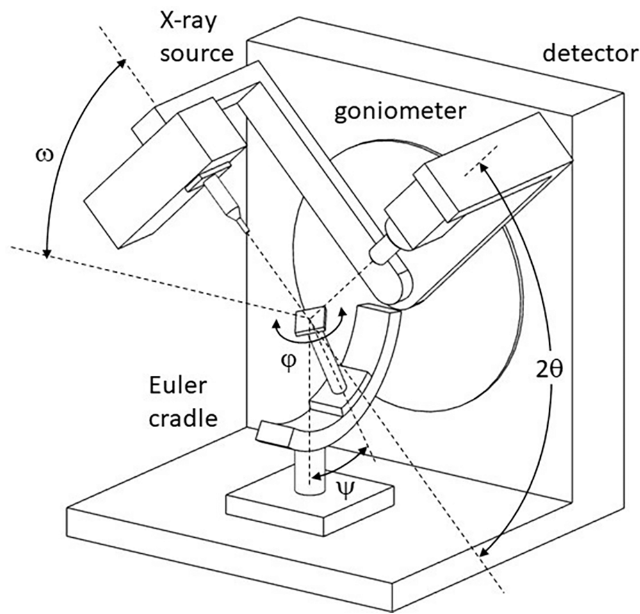

Fig. 2. Scheme of the four-circle diffractometer.

angle of incidence, in the 190–2500 nm range.

3. Results

3.1. Morphology

Fig. 3(a)-(d) shows the AFM surface images of AZO thin films grown on STO(1 1 0). The surface is characterized by uniform grains that are densely packed, implying a three-dimensional island growth mode, consistent with previous literature [27,33]. The surface morphology is not particularly influenced by the substrate: images of the AZO/SiO_2 films can be seen in Figure S1 of the Supporting Information (SI). The results of the grain analysis and surface roughness are summarized in Fig. 3(e). We observe that surface roughness and mean radius of grains increase with thickness almost linearly. The results are similar for AZO films grown on SiO_2, with the 50 nm and 100 nm thick films having a slightly smaller roughness and mean radius of grains.

3.2. Crystalline structure

Fig. 4(a) reports the 2θ-ω scans for the 300 nm film of AZO on STO (1 1 0). The scans have been recorded at a small (<0.1°) but not zero offset angle (θ-ω), in order to reduce the intensity of the substrate peaks, i.e. STO(1 1 0) and STO(2 2 0). The lack of any ZnO peak apart from ZnO (0002) and ZnO(0004) (please note the logarithmic intensity scale, spanning four orders of magnitude) demonstrate the strong preferential c-axis orientation of the AZO grains, already observed on other substrates [30,34].

The epitaxial relationship between the substrate and the film has been assessed by measuring pole figures of substrate and film Bragg reflections from planes that cut the STO(1 1 0) plane at an angle, namely STO(2 0 0) and ZnO $(\overline{1}101)$ (and symmetry equivalent planes). The substrate reflections (2θ = 46.485°, PDF 00–035-0734, [35]) are expected at tilt ψ = 45° (angle between the [1 1 0] and the [2 0 0] directions in a cubic structure), with a periodicity in ϕ of 180°, corresponding to the two-symmetry equivalent STO(2 0 0) and STO(0 2 0) crystal planes. The pole figure in Fig. 4(b) shows such two substrate reflections at ψ = 45° with the expected ϕ periodicity. We used these two reflections to set the azimuthal ϕ axis of the substrate to zero. The substrate spots are elongated in the tilt direction due to the asymmetric X-ray beam cross section that emerges from the Göbel mirror. The reflections from ZnO $(\overline{1}101)$ and symmetry equivalent planes (2θ = 36.253°) are expected at tilt ψ = 61.6°, i.e. the angle between the [0001] and the normal to the $(\overline{1}101)$ plane of the hexagonal structure, which can be calculated as $cos(\psi) = (1 + 4c^2/3a^2)^{\frac{1}{2}}$, where a = 3.2498 Å and c = 5.2066 Å are the lattice constants of the ZnO structure (PDF 00–036-1451, [36]). The pole figure shows that the ZnO $(\overline{1}101)$ and symmetry equivalent reflections are found at the expected tilt angle and with the expected 60° periodicity in ϕ, indicating that AZO forms a single hexagonal and epitaxial phase. Furthermore, the occurrence at the same value of ϕ of STO(2 0 0) and ZnO $(\overline{1}101)$ indicates that the in-plane directions STO [0 0 1] and ZnO $[1\overline{1}20]$ are collinear, as confirmed by the literature [31,32].

In order to obtain information about the microstructure of the AZO thin films, we performed 2θ-ω and ω scans of the ZnO(0002) peak. We analyzed them using the single line method, following the approach of De Keijser [37,38], which is based upon the fitting of a single diffraction peak with the Voigt function, in order to separate the Lorentzian contribution from the Gaussian one. The Lorentzian broadening is associated with the coherence length of the films, which is defined as the average extension of the crystal lattice regions which scatter coherently, i.e. those regions which are free of macroscopical defects like grain boundaries. Instead, the Gaussian component is linked to the broadening due to microstrain, i.e. lattice strain from displacements of the unit cells about their lattice positions due to defects, and tilt, that is out-of-plane rotation of the grains perpendicular to the surface normal [39,40]. Analyzing the broadening of the 2θ-ω peaks, the vertical coherence length L_z and the microstrain ε can be retrieved, while the ω peaks give the lateral coherence length L_x and the tilt α. The terms vertical and lateral are related to the directions perpendicular and parallel to the film surface, respectively. The approach is based on the Scherrer formula for the coherence lengths (Equations (2) and (3)

$$L_z = \frac{K\lambda}{\beta^L_{2\theta-\omega} cos(\theta)} \quad (2)$$

$$L_x = \frac{K\lambda}{\beta^L_{\omega} sin(\theta)} \quad (3)$$

where K is the shape factor, which is usually taken to be 0.9, λ is the X-ray wavelength and β is the integral breadth, marked by a G when it is the Gaussian integral breadth and by a L when it is the Lorentzian one. The microstrain ε is obtained via the Wilson-Stokes formula (Eq. (4)

$$\varepsilon = \frac{\beta^G_{2\theta-\omega}}{4tan(\theta)} \quad (4)$$

and the tilt α is directly measured from β^G_{ω}. The scans are shown in Fig. 5 (a) and (b), all normalized and aligned to the most intense peak which is the one of the 300 nm thick sample to better underline their different widths. The instrumental Gaussian broadening has been evaluated from the broadening of a peak of the substrate, in our case the STO(1 1 0) peak, which is close to the (0002) peak of ZnO, to minimize its dependence from the angle. The exploitation of the substrate peak allows to determine it in the same measurement run of the film, minimizing the errors in this minor correction. The results of the analysis are shown in Fig. 5(c) and (d). The numerical values are included in **Table 1 of the SI**. (0002) peaks in the 2θ-ω scans are all shifted at higher angles with respect to the (0002) ZnO bulk peak (34.422°, PDF 00–036-1451, [36]), from 34.502° at 30 nm to 34.486° at 300 nm (values are reported in **Table 1 in the SI**). This means that we have compressive strain along the c-axis, in accordance with an expected in-plane expansion to accommodate lattice mismatch (Fig. 1). The vertical coherence length is instead comparable with the film thickness, as expected for materials characterized by columnar growth like ZnO [27,33]. An exception is the 300 nm thick film. We want to evidence that the Scherrer equation is accurate up to coherence lengths of around 100–200 nm [41]. As a

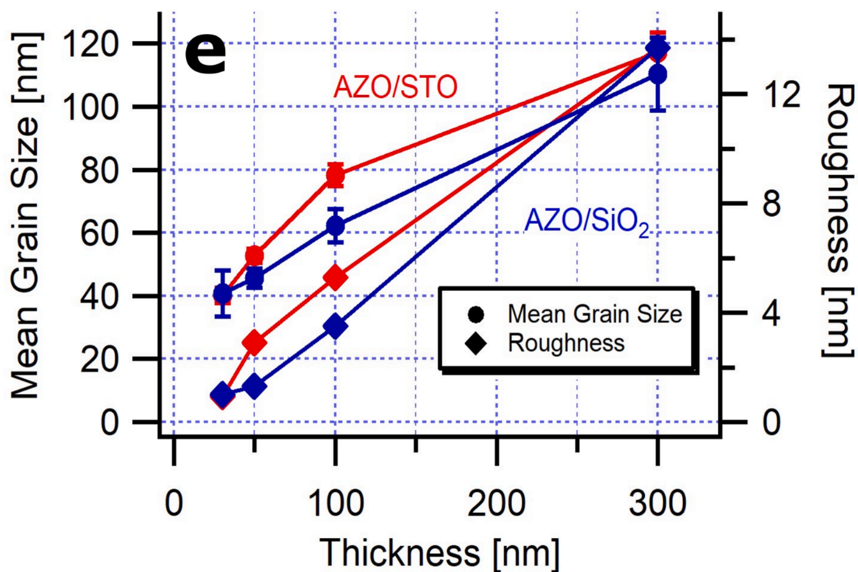

Fig. 3. AFM images (2 × 2 μm^2) of the AZO/STO films of thickness (a) 30 nm, (b) 50 nm, (c) 100 nm and (d) 300 nm. (e) Mean grain radius and roughness of AZO films. If the bar is not present, the marker size indicates the error.

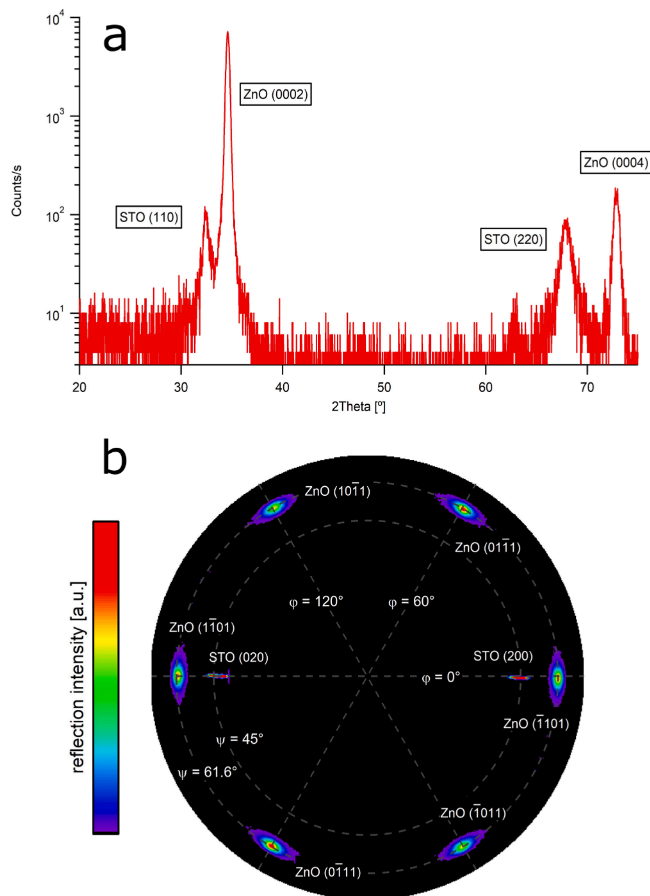

Fig. 4. (a) 2θ-ω scan of the 300 nm thick AZO/STO film. (b) Pole figure of the 300 nm AZO/STO film.

consequence, the error bar given by the fitting for this point is quite large, due to a narrow Lorentzian component. On the other hand, the lateral coherence length is almost constant at about 50 nm for all the samples, with a small decrease due to the decreasing effect of epitaxy at the interface with increasing thickness. Microstrain and tilt are in line with usual values for good quality films [42] and they decrease increasing the thickness, as expected. The same kind of analysis has been performed on AZO/SiO_2 polycrystalline films for comparison and results are shown in Fig. 6. The numerical values are included in **Table 2 of the SI**. Peaks are considerably lower with respect to AZO/STO films. We note that the vertical coherence length retains the same trend of the AZO/STO films, but is considerably smaller, proving the decrease of crystal quality with respect to epitaxial films. This fact is even more evident looking at the lateral coherence length, which is reduced to a few nm for the thinnest films and reaches a final value of 20 nm in the 300 nm thick film compared to more than 40 nm for the corresponding AZO/STO film. For polycrystalline films, the lateral coherence length has approximately a linear trend with respect to thickness, while it was almost constant for AZO/STO films. Also, microstrain and tilt are far higher with respect to epitaxial films.

3.3. Electrical measurements

To get insight on the relationship between the structural order and the electrical response of the films as a function of thickness we performed Van Der Pauw and Hall measurements. AZO/STO films show a resistivity markedly independent from thickness, as shown in Fig. 7. The same holds for carrier density and electrical Hall mobility. The average values of the electrical properties of AZO/STO films are $\rho = (4.9 \pm 1.0) \times 10^{-4}$ Ω·cm, $n = (5.1 \pm 0.5) \times 10^{20}$ cm^{-3} and $\mu_H = 26.6 \pm 3.9$ cm^2/(V·s). Instead, the AZO/SiO_2 films show a dramatic increase in resistivity as the thickness is decreased, with resistivity values even two orders of magnitude larger for the thinnest film.

3.4. Optical measurements

In Fig. 8(a) and (b), the ellipsometry spectra Δ and Ψ of AZO films deposited respectively on STO and on SiO_2, acquired with incidence angle of 60°, are presented. The ellipsometric spectra show prominent features close to the band gap region, in the near-UV (~3.8 eV). The appearance of characteristic features in the near-IR region around 0.73 eV are attributed to the bulk-plasmon resonance of the AZO films. The origin and evolution of all these features can be understood by looking at the complex dielectric function ε of the AZO films extracted from these data and presented in Fig. 8(c). The dielectric function is the physical quantity that carries all the information about the material response (band gap, polarizability, bulk plasmon resonance, and Drude contribution).

Since the dielectric functions of films of different thicknesses are almost identical, we show here only the one for 30 nm thick film, where there is the biggest difference in the electrical properties. Their dielectric functions are presented in Fig. 8(c). For modeling the optical properties of AZO we resorted to a superposition of Gaussian and so-called PSEMI oscillators [43,44] along with a Drude-type contribution for representing the doping-induced free carriers. PSEMI oscillators are parametrized functions widely employed for modeling the optical response of crystalline semiconductors. They are parametrized functions based on the Herzinger-Johs parametrized semiconductor oscillator function, that are widely employed to represent the functional form of the dielectric properties of materials. A PSEMI oscillator consists of four polynomial functions smoothly connected end-to-end, parametrized in a way that allows to reproduce almost any conceivable feature in a dielectric function, with Kramers-Kronig consistency.

The dielectric properties of AZO/STO and AZO/SiO_2 are very similar. Starting from the UV range, the optical band gap was 3.8 eV, as was calculated from a Tauc plot. In the visible region (approximately from 2 to 3 eV) the optical absorption approaches zero as expected for TCO systems. In the near-IR region, the free-carrier contribution shows up, with a screened plasma frequency around 0.73 eV. In addition to the above, from the Drude dielectric function and the definition of plasma frequency [45], it was possible to calculate the density of the free carriers n and the mobility μ. From the fit of the experimental data shown in Fig. 8(a) and (b), a carrier density of $\sim 4 \cdot 10^{20}$ cm^{-3} and mobility of around 30 cm^2/(V·s) were extracted, consistent with the values found with electrical measurements. We underline that these values are referred to the optical mobility and the optical carrier density, which almost coincide to the electrical mobility and carrier density for AZO/STO films while they are much different for AZO/SiO_2 films.

4. Discussion

To explain these trends and clarify the role of structural order in the properties of films of decreasing thickness, we have to consider the main sources of scattering, i.e. scattering processes, in highly doped semiconductor thin films, namely ionized impurity scattering, grain-boundary scattering, surface scattering and lattice vibration scattering [46–50]. Each scattering mechanism is associated with a specific electrical mobility, which contributes to the total Hall mobility of the films μ_H via Matthiessen's rule (Eq. (5), that holds if each scattering channel can be considered independent from the others

$$\frac{1}{\mu_H} = \frac{1}{\mu_{imp}} + \frac{1}{\mu_{grain}} + \frac{1}{\mu_{surf}} + \frac{1}{\mu_{lat}} \tag{5}$$

where μ_{imp} is the ionized impurity scattering mobility, μ_{grain} is the grain-boundary scattering mobility, μ_{surf} is the surface scattering mobility and

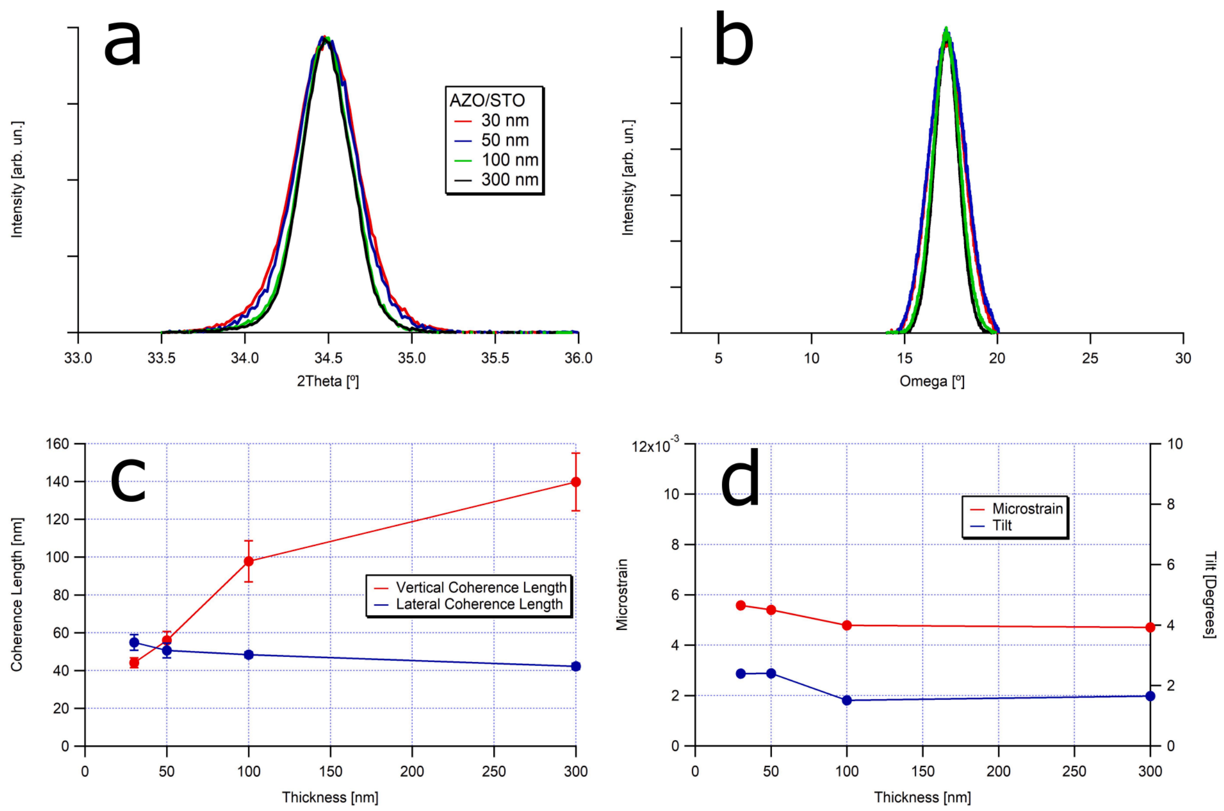

Fig. 5. (a) 2θ-ω and (b) ω scans of the (0002) ZnO peak, (c) coherence lengths, (d) microstrain and tilt for AZO/STO films. Peaks have been normalized and aligned to the most intense one, which is the one of the 300 nm thick film. If the bar is not present, the marker size indicates the error.

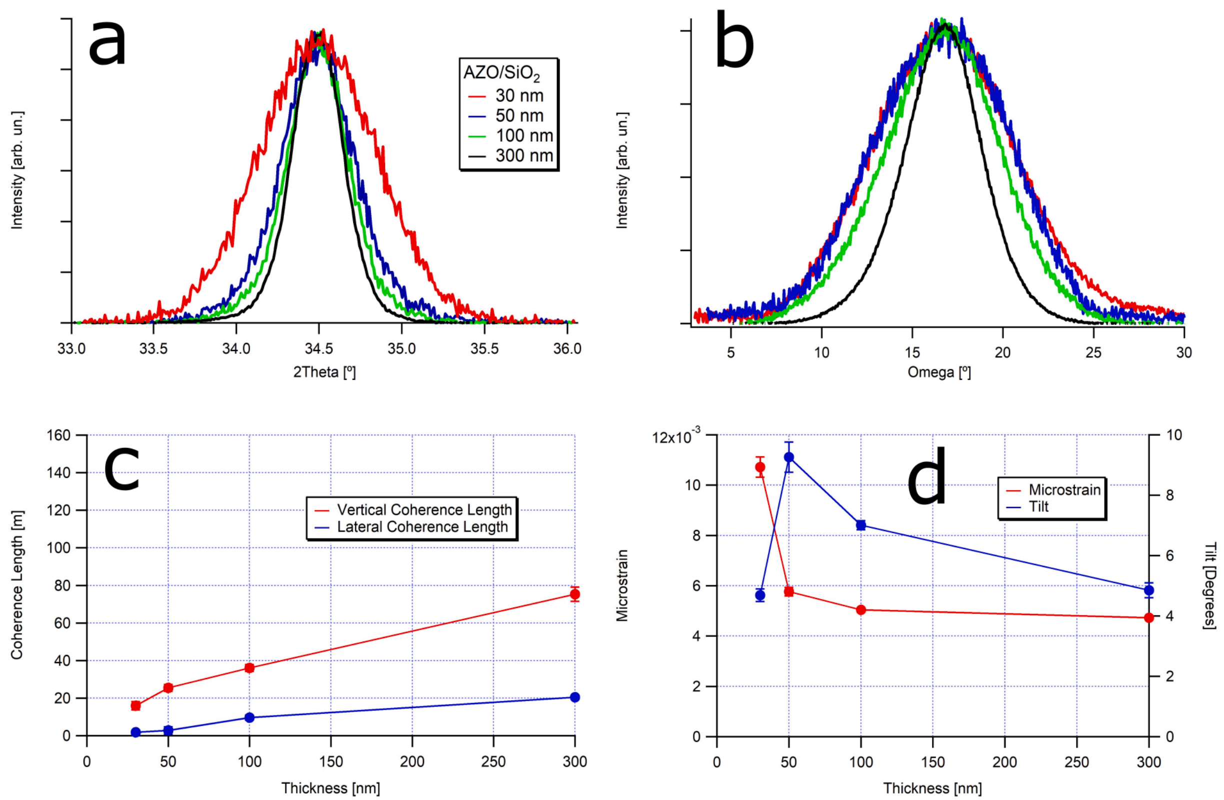

Fig. 6. (a) 2θ-ω and (b) ω scans of the (0002) ZnO peak, (c) coherence lengths and (d) microstrain and tilt for AZO/SiO_2 films. Peaks have been normalized and aligned to the most intense one, which is the one of the 300 nm thick film. If the bar is not present, the marker size indicates the error.

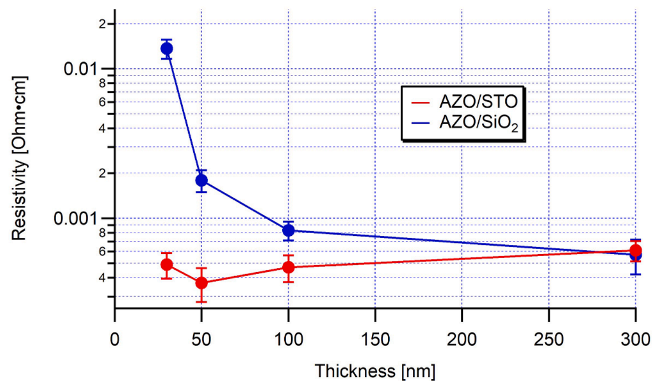

Fig. 7. Resistivity of the AZO/STO films (red) and of the AZO/SiO_2 films (blue).

μ_{lat} lattice vibration scattering mobility. The lattice vibration scattering is dominant in the high-temperature range and its contribution should be negligible at room temperature [47]. Nevertheless, it can be taken into account by considering the lattice mobility of pure ZnO, i.e. 210 $cm^2/(V\cdot s)$ [49].

The resistivity due to surface scattering in thin films depends on thickness and it can be estimated via the Fuchs-Sondheimer model [51,52], but since the resistivity of AZO/STO films is independent on thickness, surface scattering cannot contribute significantly to the mobility, and the same should be true in AZO/SiO_2 films, since they have the same thicknesses.

The mobility due to ionized impurity scattering can be evaluated via the Pisarkiewicz model [49,53], that is a modified version of the classic Brooks–Herring–Dingle (BHD) theory for a degenerate semiconductor based on the screened Coulomb potential [54,55]. The Pisarkiewicz model, which takes into account the non-parabolicity of the conduction band that was shown to be important in highly doped AZO [56–58], better fits the mobility data for degenerate semiconductors than the BHD model [49]. According to the Pisarkiewicz model, μ_{imp} can be written as

$$\mu_{imp} = \frac{3(\varepsilon_r\varepsilon_0)^2 h^3}{Z^2 m^{*2} e^3}\frac{n_e}{N_i}\frac{1}{F(\xi)} \tag{6}$$

where ε_r is the relative dielectric constant, ε_0 is the vacuum permittivity, h is the Planck constant, e is the electron charge, Z is the charge state of the impurity (for Al atoms in ZnO is 1, but at very high dopant concentrations it has to be taken into account that the impurities assemble into clusters with a larger electronic charge Z greater than 1 and a reduced concentration of scattering centers $N_i^{'} = N_i / Z$ [49,50]), m^* is the electron effective mass, N_i is the impurity concentration, which may be assumed equal to the electron density n_e for an uncompensated fully ionized semiconductor (this can always be assumed at room temperature), and $F(\xi)$ is

$$F(\xi) = \left[1 + \frac{4\xi_{np}}{\xi}\left(1 - \frac{\xi_{np}}{8}\right)\right] ln(1+\xi) - \frac{\xi}{1+\xi} - 2\xi_{np}\left(1 - \frac{5\xi_{np}}{16}\right) \tag{7}$$

where

$$\xi = \left(3\pi^2\right)^{\frac{1}{3}} \frac{\varepsilon_r\varepsilon_0 h^2 n_e^{\frac{1}{3}}}{m^* e^2} \tag{8}$$

and

$$\xi_{np} = 1 - \frac{m_0^*}{m^*} \tag{9}$$

where $m_0{}^*$ is the effective mass at the conduction band minimum. The dependence of the effective mass on the electron energy E relative to the conduction band edge E_C in the conduction band can be in fact approximated by

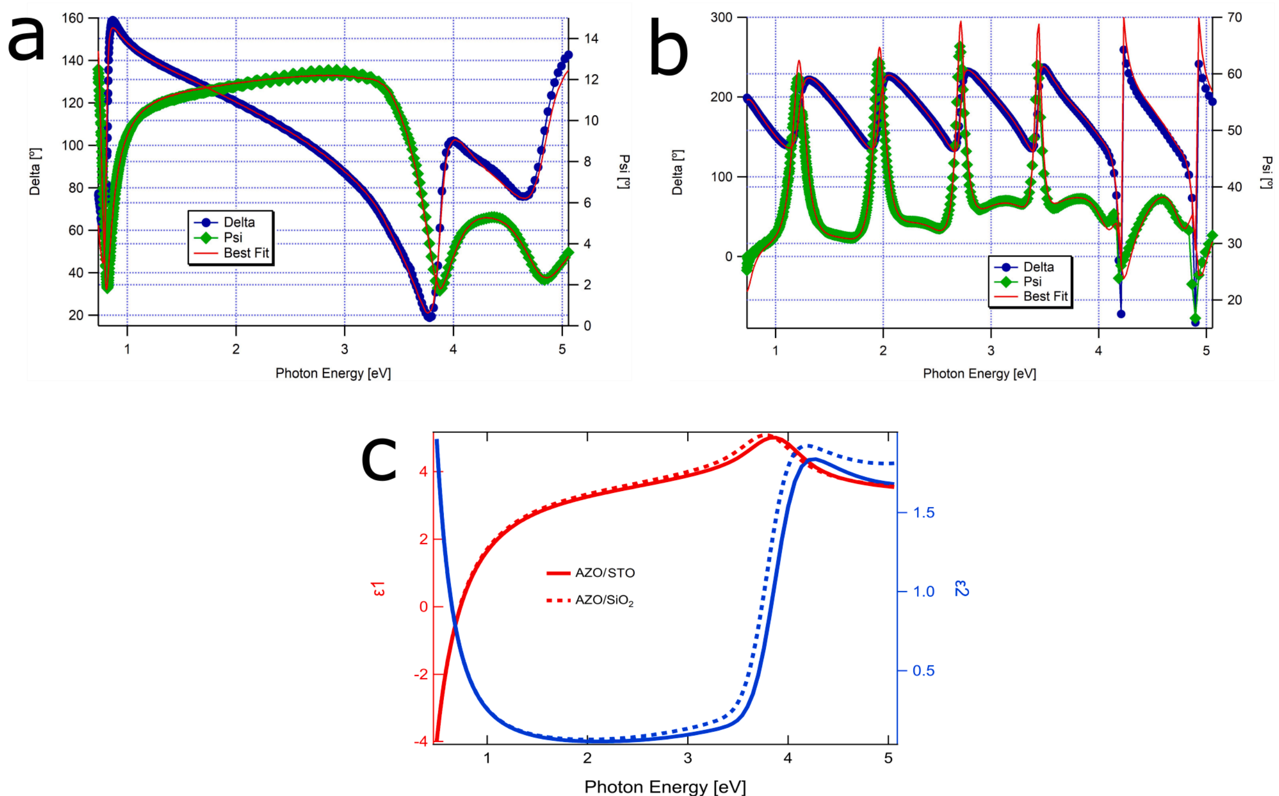

Fig. 8. (a) Ellipsometric angles for the 30 nm thick AZO/STO film with best fit. (b) Ellipsometric angles for the 30 nm thick AZO/SiO_2 film with best fit. (c) Real (ε_1) and imaginary part (ε_2) of the dielectric function of 30 nm thick AZO/STO film (full curve) and AZO/SiO_2 film (dashed curve).

$$m^{*} = m_0^{*}[1 + 2C(E - E_c)] \quad (10)$$

where C is called the non-parabolicity parameter. For the high dopant concentrations observed in this system, the electron gas is completely degenerated, and the Fermi energy is calculated as

$$E_F = \frac{1}{2C}\left[\sqrt{1 + 2C\frac{h^2}{4\pi^2 m_0^{*}}(3\pi^2 n_e)^{\frac{2}{3}}} - 1\right] \quad (11)$$

Then, the effective mass dependence on the carrier density can be written as

$$m^{*} = m_0^{*}\sqrt{1 + 2C\frac{h^2}{4\pi^2 m_0^{*}}(3\pi^2 n_e)^{\frac{2}{3}}} \quad (12)$$

The effective electron mass for AZO was reported to be in a range between $0.24m_e - 0.28m_e$, depending on the source [49,57,59–62], so we took $0.26m_e$. The relative dielectric constant of AZO thin films was taken to be 7.8 [60], which is the value of the static permittivity in the direction perpendicular to the c-axis, which is the direction along which conduction takes place since the films are c-axis oriented, while the non-parabolicity parameter was taken to be 0.56 eV^{-1}, which seems to be the most reasonable value looking at the literature [50,59]. Z has been set to 1.2, following the work of Ellmer and coworkers, and takes into account the fraction of donated electrons that are trapped due to the clustering of impurities and to the presence of oxygen vacancies and do not contribute to conductivity, together with the fact that the presence of clustering determines a reduction of the concentration of the scattering centers [50]. With our mean carrier density of $5.1 \cdot 10^{20}$ cm^{-3} we obtain a μ_{imp} of around 44 $cm^2/(V{\cdot}s)$ for epitaxial AZO/STO films. This contribution does not take into consideration the presence of compensating Zn vacancies, which are always present in AZO [63]. To account for them a compensating factor is typically included in the model [64]. However, this compensation does not significantly change this quantitative evaluation within the error of the considered approximations and is negligible compared to the other terms. Since we do not have a reliable estimation of the compensating vacancies in our films and because of the negligible correction, we decide to set the compensating factor to 0.

The last contribution to take into consideration is grain boundary scattering, that also accounts for the fraction of electrons trapped at these sites. A possible way to evaluate its contribution to mobility is the Seto model [65], where it is postulated that defects at grain boundaries induce trap states in the band gap with an areal concentration N_t. Upon occupation by electrons, these trap states form potential barriers, which have to be surmounted by the charge carriers during electron transport. Seto model can be extended to degenerate conditions [50], and μ_{grain} can be written as

$$\mu_{grain} = \frac{4\pi e m^{*} L_x k_B T}{n_e h^3} ln\left(1 + e^{\eta - \frac{E_B}{k_B T}}\right) \quad (13)$$

where L_x is the lateral grain size (our lateral coherence length), k_B is the Boltzmann's constant, T is the temperature, E_B is the potential barrier height and η is the reduced Fermi energy. For electron densities above $6 \cdot 10^{18}$ cm^{-3}, η can been approximated with an error smaller than 3 % by the following formula [66]

$$\eta = \sqrt{\left(\frac{3\sqrt{\pi}}{4}\frac{n_e}{N_c}\right)^{\frac{4}{3}} - \frac{\pi^2}{6}} \quad (14)$$

where N_C is the effective conduction band density of states, that is

$$N_C = \frac{2}{h^3}(2\pi m^{*} k_B T)^{\frac{3}{2}} \quad (15)$$

The grain barrier height is given by

$$E_B = \frac{e^2 L_x^2 n_e}{8\varepsilon_r \varepsilon_0} \quad \text{for } L_x n_e < N_t \quad (16)$$

$$E_B = \frac{e^2 N_t}{8\varepsilon_r \varepsilon_0 n_e} \quad \text{for } L_x n_e > N_t \quad (17)$$

Since N_t is in the range $1 \cdot 10^{13}$ cm^{-2} –$5 \cdot 10^{13}$ cm^{-2} in doped ZnO [50,67–69] and L_x for the AZO/STO films is around 50 nm, we fall in the second case. Taking an average N_t of $3 \cdot 10^{13}$ cm^{-2}, we obtain a μ_{grain} of around 200 $cm^2/(V \cdot s)$, which is a small contribution with respect to ionized impurity scattering in epitaxial AZO/STO films but can account for the decrease to about 25 $cm^2/(V \cdot s)$, considering also the contribution from the lattice.

Via Matthiessen's rule, we can put all these contributions together to explain the measured mobilities of AZO/STO films. Fig. 9 shows the experimental electrical mobility compared to that evaluated from Pisarkiewicz and Seto models with the measured carrier densities and lateral coherence length, plus the contribution from the lattice. The error bar on the latter is calculated by propagating the error on the carrier density. The values are all compatible within the error bars: the good agreement between experiment and models proves that in our epitaxial AZO/STO films the electrical Hall mobility is mostly limited by ionized impurity scattering, while grain boundary scattering and lattice mobility are smaller contributions. For this reason no variation is evident with decreasing thickness and thinner films maintain the same electrical response of thicker bulk-like films.

As a comparison, AZO/SiO_2 polycrystalline films grown in the same conditions and with the same thickness show a decreasing resistivity as a function of thickness. Optical mobility and optical carrier density are very similar between AZO/STO and AZO/SiO_2 films. This means that the different crystalline quality does not affect too much the intrinsic properties of the material inside grains even at reduced thickness, but affects their ability to contribute to conduction, because of grain boundary scattering. During optical excitation, there is only a slight oscillation of carriers around their equilibrium positions, so that most of them do not have to overcome the potential barriers at grain boundaries. Hence, it is only from the electrical point of view that we observe a difference between epitaxial and polycrystalline films. In fact, as already noted by Bikowski and Ellmer [67], optical and electrical measurements show nearly the same mobility values when the electron transport is limited by ionized impurity scattering and not by grain boundary scattering. For this reason in AZO/SiO_2 polycrystalline films the increasing trend of the resistivity when the thickness is reduced is expected to be associated with grain boundary scattering, since the lateral coherence length follows an opposite trend and becomes extremely small in comparison to that of epitaxial films in the thinnest films.

We can apply the same model exploited for epitaxial AZO films with polycrystalline films, using the optical carrier density obtained by

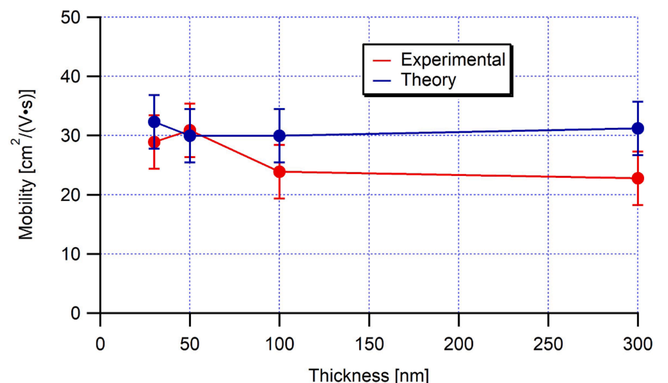

Fig. 9. Electrical Hall mobility of the AZO/STO films as measured (red) and calculated (blue).

spectroscopic ellipsometry modelling, including contributions from ionized impurity scattering via Pisarkiewicz model, from grain boundary scattering via Seto model and from lattice mobility. The similar behavior of optical and electrical carrier concentration has been demonstrated in previous studies on TCO [9,70] and recently on AZO [71], and assumed in several works on ellipsometry [72,73]. In principle one can easily switch from mobility μ to resistivity ρ by the simple relation

$$\rho = \frac{1}{ne\mu} \tag{18}$$

If we evaluate the resistivity in this way, we obtain values which are very close to the experimental ones, as shown in Fig. 10. Since the only contribution which is varying between films of different thicknesses and can justify a variation of resistivity is the lateral coherence length, this agreement is indicating that grain boundary scattering is the dominant contribution. The only point with a bad agreement is the one at 30 nm thickness. In this case however the lateral coherence length is affected by a big relative error because of its small value and thus it is at the resolution limit of XRD. This big relative error is reflected on a big uncertainty on the calculated resistivity value, that is however consistent with the experimental value.

The contribution to resistivity due solely to grain boundary scattering can be also modeled via the Mayadas-Shatzkes model [74,75]. According to the Mayadas-Shatzkes model, the resistivity ρ_{grain} of a polycrystalline film for which the influence of surface scattering can be neglected can be evaluated as

$$\frac{\rho_0}{\rho_{grain}} = 1 - \frac{3}{2}a + 3a^2 - 3a^3 ln\left(1 + \frac{1}{a}\right) \tag{19}$$

where

$$a = \frac{l_0}{D}\frac{R}{1 - R} \tag{20}$$

where ρ_0 and l_0 are the conductivity and the electron mean-free path inside a grain (i.e., the conductivity and mean-free path of a single crystal of the same material, which has the same density of defects and impurities as a grain), R is the grain boundary reflection coefficient and D is the average grain size, which in our case is the lateral coherence length L_x. The electron mean-free path l_0 [46–48] can be evaluated via Eq. (21)

$$l_0 = \left(\frac{h}{2e}\right)\left(\frac{3n_e}{\pi}\right)^{\frac{1}{3}}\mu_H \tag{21}$$

We took ρ_0 and l_0 respectively as $4.9 \cdot 10^{-4}\ \Omega \cdot$ cm and 6 nm, that are the mean values of resistivity and electron mean-free path for AZO/STO films, where grain boundary scattering can be neglected in first approximation, and thus we can take these values as the intragrain characteristics of the films. We fitted the resistivity experimental values of AZO/SiO_2 films as a function of their lateral coherence length with the Mayadas-Shatzkes model, letting the grain boundary reflection coefficient R free. The best fit is shown in Fig. 10, together with the calculated resistivity via Pisarkiewicz and Seto models. We observe a good agreement of the model considering a grain boundary reflection coefficient of approximately 0.5, which is in accordance with the literature [76]. Also, the only point for which the fit is not very close to the measure (but still in the error bar) is the one referring to the 30 nm thick AZO/SiO_2 film, because of the aforementioned resolution limit of XRD. The Mayadas-Shatzkes curve is also consistent with the previously calculated resistivity, proving once more that grain boundary scattering is the dominant contribution to resistivity for polycrystalline AZO films. These results are consistent with previous studies, where thin polycrystalline TCO films show lower crystalline quality and smaller grain sizes with respect to thicker ones, enhancing grain boundary scattering and resistivity [77]. It was reported for instance that electrical properties of Ta:TiO_2 film degrades very fast below 50 nm of thickness, with resistivity of the order of 10^{-1}-10^{-2} Ω·cm and mobilities of few $cm^2/(V \cdot s)$ for 20 nm thick films [14], and a similar behavior was observed also for ultrathin ITO films [15]. On the contrary, when a buffer layer is introduced or the interfacial quality is controlled and optimized, the mobility of charge carriers remains higher than 20 $cm^2/(V \cdot s)$ and constant down to 20 nm thickness, comparable to our results [7].

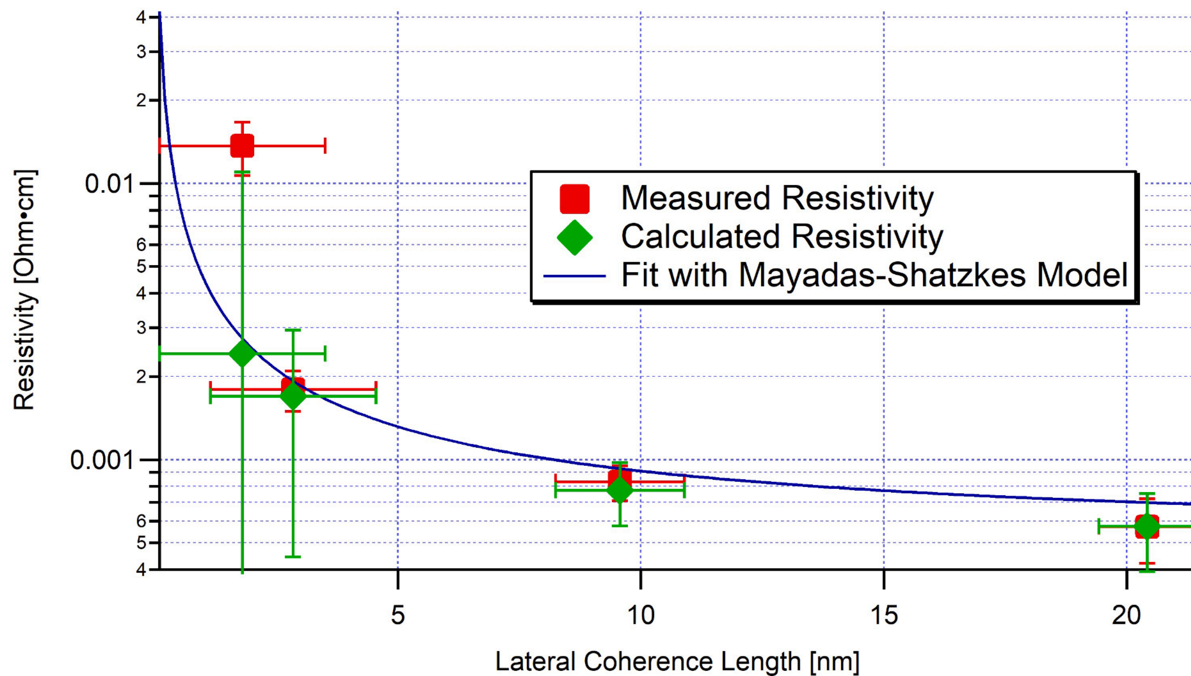

Fig. 10. Measured resistivity (red markers) of the AZO/SiO_2 films vs lateral coherence length, fitted with the Mayadas-Shatzkes model. Green markers represent the resistivity calculated via the combination of Pisarkiewicz and Seto models plus the contribution from the lattice, considering the corresponding measured lateral coherence lengths.

5. Conclusions

In conclusion, we reported an exhaustive study about RF magnetron sputtering growth of epitaxial 4 at. % AZO films as a function of thickness on STO (1 1 0) substrates and their comparison with polycrystalline films grown in the same conditions on thermal SiO_2 on Si (0 0 1) substrates. We grew films in a thickness range from 30 to 300 nm.

While the surface morphology of the films is similar, as underlined by AFM, XRD measurements proved that AZO/STO films grow epitaxial, and they display far higher crystalline quality with respect to polycrystalline films. In particular, epitaxial films show a constant lateral coherence length with respect to thickness, while polycrystalline ones show a monotonous decrease with decreasing thickness, as well as higher values of microstrain and tilt.

Electrical measurements point out that epitaxial films retain their optimal properties down to thicknesses as low as 30 nm, while polycrystalline films are considerably more resistive at low thicknesses. In contrast, no evident differences were found from an optical point of view.

These features were explained by acknowledging that, in epitaxial AZO films, grain boundary scattering is a far lesser contribution to mobility with respect to ionized impurity scattering, because of their large lateral coherence length. Hence, their electrical Hall mobility is limited mostly by ionized impurity scattering, and that copes with their constant resistivity as a function of thickness. This conclusion is corroborated by the fact that the mobility evaluated thanks to a combination of Pisarkiewicz and Seto models, where the most important contribution comes from ionized impurity scattering, and Matthiessen's rule is consistent with the measured one.

In polycrystalline films, instead, grain boundary scattering is dominant at low thicknesses and this enhances resistivity, whose trend was successfully fitted by the Mayadas-Shatzkes model. Optical properties do not show significant differences between epitaxial and polycrystalline films neither as a function of thickness, confirming that the intrinsic properties of the material inside the grains is not affected by crystal quality and grain boundary scattering is the main reason behind the degradation of the electrical properties in thinner polycrystalline films.

These considerations led us to conclude that epitaxy is a viable root to obtain high performing TCO thin films below 50 nm of thickness. These results could be very interesting for future applications where high-quality ultra-thin TCO films are needed or growth of AZO thin films on perovskite substrates is involved.

CRediT authorship contribution statement

Riccardo Magrin Maffei: Methodology, Formal analysis, Investigation, Data curation, Writing – original draft, Writing – review & editing. **Alessandro di Bona:** Conceptualization, Methodology, Resources, Data curation, Writing – review & editing. **Maria Sygletou:** Formal analysis, Investigation, Data curation. **Francesco Bisio:** Writing – review & editing, Supervision, Funding acquisition. **Sergio D'Addato:** Writing – review & editing, Supervision, Funding acquisition. **Stefania Benedetti:** Conceptualization, Methodology, Resources, Writing – review & editing, Supervision.

Declaration of Competing Interest

The authors declare that they have no known competing financial interests or personal relationships that could have appeared to influence the work reported in this paper.

Data availability

Data will be made available on request.

Acknowledgements

This project has received financial support from the EU Horizon 2020 research and innovation program under the Marie Skłodowska-Curie grant agreement no. 799126.

Appendix A. Supplementary material

Supplementary data to this article can be found online at https://doi.org/10.1016/j.apsusc.2023.157133.

References

[1] R.A. Afre, N. Sharma, M. Sharon, M. Sharon, Transparent conducting oxide films for various applications: a review, Rev. Adv. Mater. Sci. 53 (2018) 79–89.

[2] Y. Chen, Review of ZnO transparent conducting oxides for solar applications, IOP Conf. Ser.: Mater. Sci. Eng. 423 (2018), 012170.

[3] K. Ellmer, Past achievements and future challenges in the development of optically transparent electrodes, Nat. Photon. 6 (2012) 809–817.

[4] G.V. Naik, V.M. Shalaev, A. Boltasseva, Alternative plasmonic materials: beyond gold and silver, Nat. Photon. 25 (2013) 3264–3294.

[5] K. Ellmer, A. Klein, B. Rech, Transparent Conductive Zinc Oxide 104 (2008). Springer Series in Material Science,.

[6] T. Minami, Transparent conducting oxide semiconductors for transparent electrodes, Semicond. Sci. Tech. 20 (2005) S33–S44.

[7] D.C. Look, Mobility vs thickness in n+-ZnO films: Effects of substrates and buffer layers, Mater. Sci. Semicond. 69 (2017) 2.

[8] D.C. Look, K.D. Leedy, A. Kiefer, B. Claflin, N. Itagaki, K. Matsushima, I. Surhariadi, Model for thickness dependence of mobility and concentration in highly conductive zinc oxide, Opt. Eng. 52 (2013), 033801.

[9] D.C. Look, K.D. Leedy, D.B. Thomson, B. Wang, Defects in highly conductive ZnO for transparent electrodes and plasmonics, J. Appl. Phys. 115 (2014), 012002.

[10] J. Yoon, S. Jo, I.S. Chun, I. Jung, H.-S. Kim, M. Meitl, E. Menard, X. Li, J. J. Coleman, U. Paik, J.A. Rogers, GaAs photovoltaics and optoelectronics using releasable multilayer epitaxial assemblies, Nature 465 (2010) 329–334.

[11] M. Sygletou, F. Bisio, S. Benedetti, P. Torelli, A. di Bona, A. Petrov, M. Canepa, Transparent conductive oxide-based architectures for the electrical modulation of the optical response: a spectroscopic ellipsometry study, J. Vac. Sci. Technol. B 37 (2019), 061209.

[12] E. Bellingeri, I. Pallecchi, L. Pellegrino, G. Canu, M. Biasotti, M. Vignolo, A.S. Siri, D. Marré, Crystalline ZnO/SrTiO3 transparent field effect transistor, Phys. Status Solidi A 205 (2008) 1934–1937.

[13] Q. Liu, F. Jin, J. Dai, B. Li, L. Geng, J. Liu, Effect of thickness on the electrical and optical properties of epitaxial (La0.07Ba0.93)SnO3 thin films, Superlattices Microstruct. 96 (2016) 205–211.

[14] B.R. Bricchi, M. Sygletou, L. Ornago, G. Terraneo, F. Bisio, C. Mancarella, L. Stasi, F. Rusconi, E. Mogni, M. Ghidelli, P. Biagioni, A.L. Bassi, Optical and electronic properties of transparent conducting Ta:TiO2 thin and ultra-thin films: the effect of doping and thickness, Mater. Adv. 2 (2021) 7064–7076.

[15] J. Gwamuri, A. Vora, R.R. Khanal, A.B. Phillips, M.J. Heben, D.O. Güney, P. Bergstrom, A. Kulkarni, J.M. Pearce, Limitations of ultrathin transparent conducting oxides for integration into plasmonic enhanced thin-film solar photovoltaic devices, Mater. Renew. Sustain. Energy 4 (2015) 12.

[16] D.Y. Kang, B.-H. Kim, T.H. Lee, J.W. Shim, S. Kim, H.-J. Sung, K.J. Chang, T. G. Kim, Dopant-tunable ultrathin transparent conductive oxides for efficient energy conversion devices, Nano-Micro Lett. 13 (2021) 211.

[17] A. Sytchkova, D. Zola, L. Bailey, B. Mackenzie, G. Proudfoot, M. Tian, A. Ulyashin, Depth dependent properties of ITO thin films grown by pulsed DC sputtering, Mater. Sci. Eng. B 178 (2013) 586.

[18] T. Minami, T. Miyata, Present status and future prospects for development of non- or reduced-indium transparent conducting oxide thin films, Thin Solid Films 517 (2008) 1474.

[19] A. Vora, J. Gwamuri, J.M. Pearce, P.L. Bergstrom, D.O. Güney, Multi-resonant silver nano-disk patterned thin film hydrogenated amorphous silicon solar cells for Staebler-Wronski effect compensation, J. Appl. Phys. 116 (2014), 093103.

[20] L.M. Trinca, A.C. Galca, G. Aldica, R. Radu, I. Mercioniu, L. Pintilie, On the growth of conductive aluminum doped zinc oxide on 001 strontium titanate single crystals, Appl. Surf. Sci. 364 (2016) 365–370.

[21] P. Mele, S. Saini, H. Honda, K. Matsumoto, K. Miyazaki, H. Hagino, A. Ichinose, Effect of substrate on thermoelectric properties of Al-doped ZnO thin films, Appl. Phys. Lett. 102 (2013), 253903.

[22] X.H. Wei, Y.R. Li, J. Zhu, W. Huang, Y. Zhang, W.B. Luo, H. Ji, Epitaxial properties of ZnO thin films on SrTiO3 substrates grown by laser molecular beam epitaxy, Appl. Phys. Lett. 90 (2007), 151918.

[23] X.H. Wei, Y.R. Li, W.J. Jie, J.L. Tang, H.Z. Zeng, W. Huang, Y. Zhang, J. Zhu, Heteroepitaxial growth of ZnO on perovskite surfaces, J. Phys. D: Appl. Phys. 40 (2007) 7502–7507.

[24] P. Kuppusami, G. Vollweiler, D. Rafaja, K. Ellmer, Epitaxial growth of aluminium-doped zinc oxide films by magnetron sputtering on (001), (110), and (012) oriented sapphire substrates, Appl. Phys. A 80 (2005) 183–186.

[25] J.-Y. Hwang, C. Cho, L. Sang-A, S.-Y. Jeong, Epitaxial growth and structural characterization of transparent conducting ZnO: Al thin film deposited on GaN substrate by RF magnetron sputtering, J. Korean Phys. Soc. 47 (2005) 288–291.
[26] V.P. Vlasov, A.V. Butashin, V.M. Kanevskii, A.E. Muslimov, V.A. Babaev, A. M. Ismailov, M.K. Rabadanov, Suppression of growth domains in epitaxial ZnO films on structured (0001) sapphire surface, Cryst. Rep. 59 (2014) 422–424.
[27] S.H. Seo, H.C. Kang, Effect of sputtering pressure on growth behavior of heteroepitaxial ZnO/SrTiO3 (001) films grown by radio frequency magnetron sputtering, Mater. Lett. 98 (2013) 131–134.
[28] E.M. Kaidashev, M. Lorenz, H. von Wenckstern, A. Rahm, H.-C. Semmelhack, K.-H. Han, G. Benndorf, C. Bundesmann, H. Hochmuth, M. Grundmann, High electron mobility of epitaxial ZnO thin films on c-plane sapphire grown by multistep pulsed-laser deposition, Appl. Phys. Lett. 82 (2003) 3901.
[29] H. Tampo, A. Yamada, P. Fons, H. Shibata, K. Matsubara, K. Iwata, S. Niki, K. Nakahara, H. Takasu, Degenerate layers in epitaxial ZnO films grown on sapphire substrates, Appl. Phys. Lett. 84 (2004) 4412.
[30] I. Valenti, S. Benedetti, A. di Bona, V. Lollobrigida, A. Perucchi, P.D. Pietro, S. Lupi, S. Valeri, P. Torelli, Electrical, optical, and electronic properties of Al:ZnO films in a wide doping range, J. Appl. Phys. 118 (2015), 165304.
[31] E. Bellingeri, D. Marré, I. Pallecchi, L. Pellegrino, A.S. Siri, High mobility in ZnO thin films deposited on perovskite substrates with a low temperature nucleation layer, Appl. Phys. Lett. 86 (2005), 012109.
[32] E. Bellingeri, D. Marré, L. Pellegrino, I. Pallecchi, G. Canu, M. Vignolo, C. Bernini, A.S. Siri, High mobility ZnO thin film deposition on SrTiO3 and transparent field effect transistor fabrication, Superlattices Microstruct. 38 (2005) 446–454.
[33] J.W. Shin, J.Y. Lee, T.W. Kima, Y.S. No, W.J. Cho, W.K. Choi, Growth mechanisms of thin-film columnar structures in zinc oxide on p-type silicon substrates, Appl. Phys. Lett. 88 (2006), 091911.
[34] K. Matsubara, P. Fons, A. Yamada, M. Watanabe, S. Niki, Epitaxial growth of ZnO thin films on LiNbO3 substrates, Thin Solid Films 347 (1999) 238–240.
[35] H. Swanson, H. Fuyat, Natl. Bur. Stand. (U.S.), Circ. 539 3 (1954) 44.
[36] H.F. McMurdie, M.C. Morris, E.H. Evans, B. Paretzkin, W. Wong- Ng, L. Ettlinger, C.R. Hubbard, Powder Diffr. 1 (1986) 76.
[37] T.H. de Keijser, J.I. Langford, E.J. Mittemeijer, A.B.P. Vogels, Use of the Voigt function in a single-line method for the analysis of X-ray diffraction line broadening, J. Appl. Cryst. 15 (1982) 308–314.
[38] R. Delhez, T.H.D. Keijser, E.J. Mittemeijer, Determination of crystallite size and lattice distortions through X-ray diffraction line profile analysis, Z. Anal. Chem. 312 (1982) 1–16.
[39] T. Metzger, R. Höpler, E. Born, O. Ambacher, M. Stutzmann, R. Stömmer, M. Schuster, H. Göbel, S. Christiansen, M. Albrecht, H.P. Strunk, Defect structure of epitaxial GaN films determined by transmission electron microscopy and triple-axis X-ray diffractometry, Philos. Mag. A 77 (4) (1998) 1013–1025.
[40] R. Chierchia, T. Böttcher, H. Heinke, S. Einfeldt, S. Figge, D. Hommel, Microstructure of heteroepitaxial GaN revealed by x-ray diffraction, J. Appl. Phys. 93 (2003) 8918.
[41] P. Scherrer, Nachr Ges Wiss Goettingen, Math. Phys. 2 (1918) 98–100.
[42] D. Singh, R. Kumar, T. Ganguli, S.S. Major, High resolution x-ray diffraction study of the substrate temperature and thickness dependent microstructure of reactively sputtered epitaxial ZnO films, Mater. Res. Express 4 (2017), 096405.
[43] C. Herzinger, B. Johs, Guide to Using WVASE32, J.A, Woollam Company, 1996.
[44] C. Herzinger, B. Johs, Dielectric function parametric model and method of use, J.A, Woollam Company, 1998.
[45] M. Sygletou, S. Benedetti, A. di Bona, M. Canepa, F. Bisio, Doping-dependent optical response of a hybrid transparent conductive oxide/plasmonic medium, J. Phys. Chem. C 126 (2022) 1881–1889.
[46] Z.L. Pei, C. Sun, M.H. Tan, J.Q. Xiao, D.H. Guan, R.F. Huang, L.S. Wen, Optical and electrical properties of direct-current magnetron sputtered ZnO: Al films, J. Appl. Phys. 90 (2001) 3432.
[47] J.G. Lu, Z.Z. Ye, Y.J. Zeng, L.P. Zhu, L. Wang, J. Yuan, B.H. Zhao, Q.L. Liang, Structural, optical, and electrical properties of (Zn, Al)O films over a wide range of compositions, J. Appl. Phys. 100 (2006), 073714.
[48] M. Chen, Z.L. Pei, X. Wang, Y.H. Yu, X.H. Liu, C. Sun, L.S. Wen, Intrinsic limit of electrical properties of transparent conductive oxide films, J. Phys. D: Appl. Phys. 33 (2000) 2538–2548.
[49] K. Ellmer, Resistivity of polycrystalline zinc oxide films: current status and physical limit, J. Phys. D: Appl. Phys. 34 (2001) 3097–3108.
[50] A. Bikowski, K. Ellmer, Analytical model of electron transport in polycrystalline, degenerately doped ZnO films, J. Appl. Phys. 116 (2014), 143704.
[51] K. Fuchs, The conductivity of thin metallic films according to the electron theory of metals, Proc. Cambridge Philos. Soc. 34 (1938) 100–108.
[52] E.H. Sondheimer, The mean free path of electrons in metals, Adv. Phys. 1 (1952) 1–42.
[53] T. Pisarkiewicz, K. Zakrzewska, E. Leja, Scattering of charge carriers in transparent and conducting thin oxide films with a non-parabolic conduction band, Thin Solid Films 174 (1989) 217–223.
[54] R.B. Dingle, Scattering of electrons and holes by charged donors and acceptors in semiconductors, Phil. Mag. 46 (1955) 831–840.
[55] W. Zawadzki, Handbook on Semiconductors, North-Holland, Amsterdam, 1982.
[56] F. Ruske, A. Pflug, V. Sittinger, B. Szyszka, D. Greiner, B. Rech, Optical modeling of free electron behavior in highly doped ZnO films, Thin Solid Films 518 (2009) 1289–1293.
[57] J.G. Lu, S. Fujita, Carrier concentration dependence of band gap shift in n-type ZnO: Al films, J. Appl. Phys. 101 (2007), 083705.
[58] T. Minami, H. Sato, K. Ohashi, T. Tomofuji, S. Takata, Conduction mechanism of highly conductive and transparent zinc oxide thin films prepared by magnetron sputtering, J. Cryst. Growth 117 (1992) 370–374.
[59] D.L. Young, T.J. Coutts, V.I. Kaydanov, A.S. Gilmore, W.P. Mulligan, Direct measurement of density-of-states effective mass and scattering parameter in transparent conducting oxides using second order transport phenomena, J. Vac. Sci. Technol. A 18 (2000) 2978.
[60] B.K. Meyer, H. Alves, D.M. Hofmann, W. Kriegseis, D. Forster, F. Bertram, J. Christen, A. Hoffmann, M. Straßburg, M. Dworzak, U. Haboeck, A.V. Rodina, Bound exciton and donor–acceptor pair recombinations in ZnO, Phys. Stat. Sol. B 241 (2004) 231–260.
[61] W.M. Kim, I.H. Kim, J.H. Ko, B. Cheong, T.S. Lee, K.S. Lee, D. Kim, T.-Y. Seong, Density-of-state effective mass and nonparabolicity parameter of impurity doped ZnO thin films, J. Phys. D: Appl. Phys. 41 (2008), 195409.
[62] A. Calzolari, A. Ruini, A. Catellani, Transparent conductive oxides as near-IR plasmonic materials: the case of Al-Doped ZnO derivatives, ACS Photonics 1 (2014) 703–709.
[63] S. Benedetti, I. Valenti, A. di Bona, G. Vinai, C. Castan-Guerrero, S. Valeri, A. Catellani, A. Ruini, P. Torelli, A. Calzolari, Spectroscopic identification of the chemical interplay between defects and dopants in Al-doped ZnO, Phys. Chem. Chem. Phys. 19 (2017) 29364–29371.
[64] N. Sommer, J. Hupkes, U. Raw, Field Emission at Grain Boundaries: Modeling the Conductivity in Highly Doped Polycrystalline Semiconductors, Phys. Rev. Applied 5 (2016), 024009.
[65] J.Y.W. Seto, The electrical properties of polycrystalline silicon films, J. Appl. Phys. 46 (1975) 5247.
[66] J.S. Blakemore, Approximations for Fermi-Dirac integrals, especially the function F12(η) used to describe electron density in a semiconductor, Solid State Electron. 25 (1982) 1067–1076.
[67] A. Bikowski, K. Ellmer, A comparative study of electronic and structural properties of polycrystalline and epitaxial magnetron-sputtered ZnO: Al and Zn1−xMgxO: Al Films—Origin of the grain barrier traps, J. Appl. Phys. 114 (2013), 063709.
[68] K. Ellmer, G. Vollweiler, Electrical transport parameters of heavily-doped zinc oxide and zinc magnesium oxide single and multilayer films heteroepitaxially grown on oxide single crystals, Thin Solid Films 496 (2006) 104–111.
[69] K. Ellmer, R. Mientus, Carrier transport in polycrystalline transparent conductive oxides: a comparative study of zinc oxide and indium oxide, Thin Solid Films 516 (2008) 4620–4627.
[70] H. Makino, N. Yamamoto, A. Miyake, T. Yamada, Y. Hirashima, H. Iwaoka, T. Itoh, H. Hokari, H. Aoki, T. Yamamoto, Influence of thermal annealing on electrical and optical properties of Ga-doped ZnO thin films, Thin Solid Films 518 (2009) 1386–1389.
[71] M. Sygletou, S. Benedetti, A. di Bona, M. Canepa, F. Bisio, E. Bellingeri, In-Operando Optical Spectroscopy of Field-Effect-Gated Al-Doped ZnO, ACS Appl. Mater. Interfaces 15 (2023) 3112.
[72] H. Fujiwara, M. Kondo, Effects of carrier concentration on the dielectric function of ZnO: Ga and In2O3: Sn studied by spectroscopic ellipsometry: Analysis of free-carrier and band-edge absorption, Phys. Rev. B 71 (2005), 075109.
[73] J. Nomoto, H. Makino, T. Yamamoto, Carrier mobility of highly transparent conductive Al-doped ZnO polycrystalline films deposited by radio-frequency, direct-current, and radio-frequency-superimposed direct-current magnetron sputtering: Grain boundary effect and scattering in the grain bulk, J. Appl. Phys. 117 (2015), 045304.
[74] A.F. Mayadas, M. Shatzkes, Electrical-resistivity model for polycrystalline films: the case of arbitrary reflection at external surfaces, Phys. Rev. B 1 (1970) 1382–1389.
[75] A.F. Mayadas, M. Shatzkes, J.F. Janak, Electrical resistivity model for polycrystalline films: the case of specular reflection at external surfaces, Appl. Phys. Lett. 14 (1969) 345.
[76] N. Argibay, R.S. Goeke, M.T. Dugger, M.A. Rodriguez, J.R. Michael, S.V. Prasad, Electrical resistivity of Au-ZnO nanocomposite films, J. Appl. Phys. 113 (2013), 143712.
[77] T. Yamada, H. Makino, N. Yamamoto, T. Yamamoto, Ingrain and grain boundary scattering effects on electron mobility of transparent conducting polycrystalline Ga-doped ZnO films, J. Appl. Phys. 107 (2010), 123534.